# Deep-subwavelength negative-index waveguiding enabled by coupled conformal surface plasmons

**R. Quesada,[1] D. Martín-Cano,[1,2] F. J. García-Vidal,[1] and J. Bravo-Abad[1,*]**

[1]*Departamento de Física Teórica de la Materia Condensada and Condensed Matter Physics Center (IFIMAC), Universidad Autónoma de Madrid, 28049 Madrid, Spain*

[2]*Max Planck Institute for the Science of Light and Quantum Science and Technology in ARcetri (QSTAR), D-91058 Erlangen, Germany*

**Corresponding author: jorge.bravo@uam.es*

Received February 25, 2014; revised April 9, 2014; accepted April 9, 2014; posted April 9, 2014 (Doc. ID 207122); published May 14, 2014

In this Letter we introduce a novel route for achieving negative-group-velocity waveguiding at deep-subwavelength scales. Our scheme is based on the strong electromagnetic coupling between two conformal surface plasmon structures. Using symmetry arguments and detailed numerical simulations, we show that the coupled system can be geometrically tailored to yield negative-index dispersion. A high degree of subwavelength modal confinement, of $\lambda/10$ in the transversal dimensions, is also demonstrated. These results can assist in the development of ultrathin surface circuitry for the low-frequency region (microwave and terahertz regimes) of the electromagnetic spectrum. 

*OCIS codes:* (240.6680) Surface plasmons; (230.7370) Waveguides; (230.7390) Waveguides, planar; (240.6690) Surface waves; (050.6624) Subwavelength structures.
http://dx.doi.org/10.1364/OL.39.002990

Highly conducting surfaces can support *spoof surface plasmon* modes when textured at the subwavelength scale [1–4]. The unique ability of these spoof surface plasmons to emulate optical-frequency surface plasmons at much lower frequencies has opened novel routes for wave control of far-IR, microwave, and terahertz radiation [5–12]. On a different note, metasurfaces based on periodic arrays of subwavelength resonators deposited on thin films are drawing growing interest, particularly due to their potential as ultraflat optical components [13]. Recently, the versatility of these concepts has been substantially extended with the demonstration of a novel class of geometry-induced modes supported by ultrathin and flexible metal films [the so-called *conformal surface plasmons* (CSPs)] [14,15]. The simplicity of the structures supporting CSPs and their inherent design advantages (including deep-subwavelength confinement, low bending losses, and broadband operation) are bringing closer the prospect of developing practical ultrathin surface circuitry for microwave and terahertz radiation.

One of the enabling elements for the development of such technology is the realization of negative-index (negative group velocity) CSP waveguides. The realization of such waveguides would represent a further step within the general endeavor of radiation control using negative-index metamaterials [16–20] and plasmonic structures [21–23]. In this Letter, we introduce a novel strategy to achieve negative group velocity at deep-subwavelength scales in strongly coupled comb-shaped CSP structures. In particular, we show, through symmetry arguments and detailed numerical simulations, how a coupled CSP system can be geometrically tailored to obtain a band featuring negative group velocity.

Figures 1(a) and 1(b) display the two waveguiding structures considered in this work. The two structures can be viewed as alternative ways of coupling two parallel comb-shaped metallic structures supporting CSP modes. Each of these comb-shaped CSP structures consists of a metal strip of thickness $t$ perforated by a periodic array of air grooves of depth $h$ and width $a$ (the array periodicity being $d$). In the first configuration [Fig. 1(a)], the two CSP structures are arranged so that their corresponding groove openings are facing each other at a distance $g$. In the second configuration

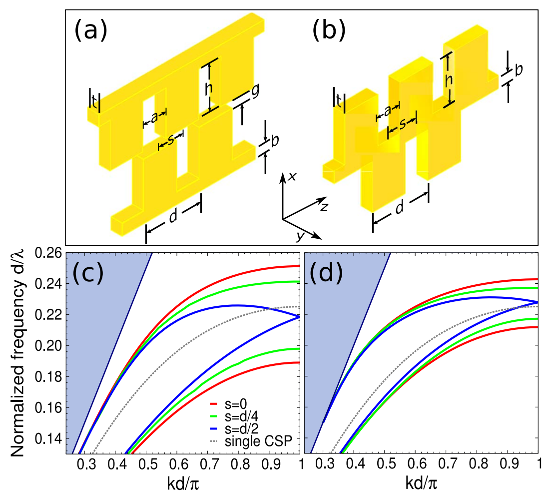


Fig. 1. (a), (b) Waveguiding structures under study, along with the definition of the corresponding geometrical parameters. In both cases the considered waveguide modes propagate along the $z$ direction (the wave vector $k$ is parallel to $z$). (c) Dispersion relation for the waveguide modes of the structure displayed in (a), as computed for the following set of geometrical parameters: $t = 0.02d$, $a = 0.4d$, $h = 0.8d$, $b = 0.2d$, and $g = 0.1d$ (where $d$ is the periodicity of the structure along $z$). The results for different values of $s$ ($s = 0$, $s = d/4$, and $s = d/2$) are displayed. (d) Same as in (c), but computed for the structure rendered in (b). In both panels the dashed gray line corresponds to a single CSP structure, while the blue shaded region in each panel represents the light cone.

 

[Fig. 1(b)], the openings of the grooves of the corrugated metal strips face opposite directions. In this latter case, the two comb-shaped structures are actually merged, so the whole structure resembles a double-width metallic strip with periodic perforations on both sides. Importantly, both waveguiding configurations feature an arbitrary lateral shift ($s$), along the $z$ direction, of one of the metallic combs with respect to the other (see the axis definitions in Fig. 1). This parameter is defined so $s = 0$ represents the case in which the grooves of the two coupled CSP structures are fully aligned [see definition of $s$ in Figs. 1(a) and 1(b)]. In fact, by applying the symmetry arguments presented in [24,25], it can be shown that this shift is an essential ingredient to achieve negative-index waveguiding. Specifically, for $s = d/2$ the analyzed structures remain invariant under a discrete periodic translation in the $z$ direction, as well as under a *glide-reflection* symmetry operation (consisting of a translation by $d/2$ followed by a reflection with respect to a $y$–$z$ plane passing through the waveguide axis). This higher symmetry forces the modal fields of the system to be eigenmodes of the corresponding discrete-translation and glide-reflection operators ($\hat{T}$ and $\hat{G}$, respectively). As shown in [24,25], from the fact that $\hat{T} = \hat{G}\hat{G}$, it follows that the eigenvalues of $\hat{G}$ are actually the two square roots of the eigenvalues $\exp(ikd)$ of $\hat{T}$ (with $k$ being the wave vector along $z$). Consequently, the wavenumber ($kd$) spectrum of eigenvalues of $\hat{G}$ must be $4\pi$ periodic (and even with respect to $kd = 0$). Considering that the $kd$ spectrum of eigenvalues of $\hat{T}$ is in fact the same as that of $\hat{G}$ plus a $2\pi$-shifted version, it follows that two bands of the dispersion diagram, displaying opposite signs of their corresponding group velocities, will cross at $kd = \pi$. The numerical demonstration and analysis of this class of symmetry-based negative-group-velocity properties in the case of coupled CSP structures is the main focus of this Letter.

The guided-mode dispersion relations, computed with the finite-element method [26], corresponding to the structures displayed in Figs. 1(a) and 1(b) are depicted in Figs. 1(c) and 1(d), respectively. In these calculations, we have fixed the geometrical parameters defining each metallic comb (following Ref. [14], we choose $t = 0.02d$, $a = 0.4d$, $h = 0.8d$, $b = 0.2d$), as well as fixing the distance between them to $g = 0.1d$. Then we have studied how the calculated bands evolve when the lateral shift $s$ is increased. Figures 1(c) and 1(d) show the results for three representative values of this lateral shift, $s = 0$, $s = d/4$, and $s = d/2$. For comparison, the dispersion relation corresponding to a single CSP structure is also displayed. In all displayed calculations the metallic parts of the structure are modeled within the perfect electric conductor (PEC) approximation.

As observed in Figs. 1(c) and 1(d), when the two metallic combs come close, the large electromagnetic coupling between them causes the dispersion relation of a single CSP structure dispersion to split into a lower- and a higher-frequency band. These two bands can be understood as the result of the *bonding* and *antibonding* combination of the highly localized waveguide modes supported by each CSP structure. Figures 1(c) and 1(d) clearly show that for large values of the wavevector $k$, the frequency splitting between the bonding and antibonding bands decreases rapidly as the shift $s$ is increased. Full degeneration of the bonding and antibonding bands is obtained at the edge of the first Brillouin zone ($k = \pi/d$) by choosing $s = d/2$. These calculations corroborate the symmetry analysis presented above. Our numerical results show that by using the geometrical parameters given above, it is possible to achieve negative index in a frequency interval spanning from $d/\lambda = 0.220$ to $d/\lambda = 0.228$ for the structure rendered in Fig. 1(a), and from $d/\lambda = 0.228$ to $d/\lambda = 0.232$ for the structure in Fig. 1(b).

We now analyze how robust the reported negative-index behavior is to the variation of the geometrical parameters characterizing the system. Of particular interest is the analysis of the dependence with the thickness $t$. Figure 2(a) displays the computed bands for the case $s = d/2$ and for several values of $t$, ranging from $t = 0.02d$ to $t = 2d$. The bands calculated for the 2D counterpart of that structure (labeled as $t \to \infty$ in the figure) are also shown. $H$ polarization is assumed in these 2D calculations. All the results correspond to the structure displayed in Fig. 1(a). We have found that all waveguiding characteristics of the structure displayed in Fig. 1(a) are similar to those corresponding to the structure of Fig. 1(b). Therefore, in the rest of this Letter we focus on the analysis of the structure in Fig. 1(a).

Figure 2(a) shows how for large $k$ values, the increase of $t$ introduces a red frequency shift in the bands. As seen in Fig. 2(a), the increase of $t$ also yields an increase of the magnitude of the negative group velocity characterizing

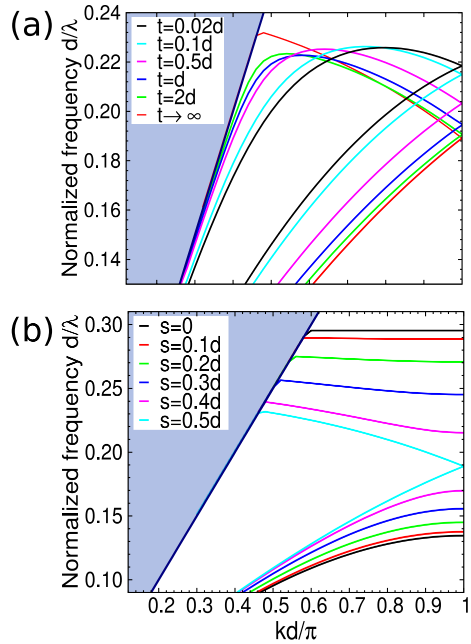


Fig. 2. (a) Dispersion relation for the waveguide modes of the structure sketched in Fig. 1(a), as computed for several values of the thickness $t$, ranging from $t = 0$ to an infinitely thick structure ($t \to \infty$). A lateral shift $s = d/2$ is assumed. The rest of the geometrical parameters are the same as in Fig. 1(c). (b) Dispersion relation for the waveguide modes ($H$-polarized) of the two-dimensional (2D) counterpart of the structure shown in Fig. 1(a). The results for different values of the lateral shift $s$ (ranging from $s = 0$ to $s = d/2$) are displayed. The blue shaded regions in both panels represent the light cone.

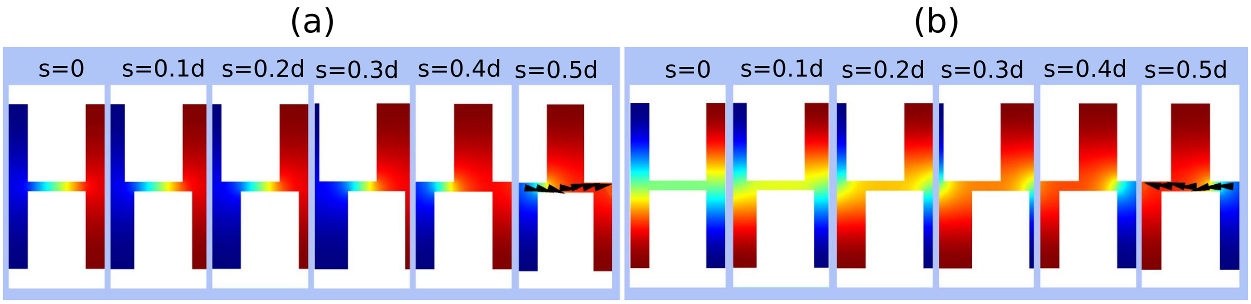


Fig. 3. (a) Magnetic field profiles (**H** pointing out of the plane) of the bonding band computed for the two-dimensional counterpart of the structure displayed in Fig. 1(a). The different panels correspond to different values of the lateral shift $s$, going from $s = 0$ (leftmost panel) to $s = d/2$ (rightmost panel). The rest of the geometrical parameters are the same as in Fig. 1(c). All the displayed cases correspond to a wavevector $k = \pi/d$. The overlaid arrows in the rightmost panel represent the direction of the Poynting vector. (b) Same as in (a), but obtained for the antibonding band.

the higher frequency band at large $k$ values. In addition, these results indicate that a value of the thickness $t = 2d$ is enough to reproduce almost completely all band characteristics of the 2D case. To check this point, we have computed the $H$-polarized bands for the 2D case [see Fig. 2(b)]. These results clearly show that a 2D model qualitatively reproduces (for large values of $k$) the whole dependence with $s$ obtained from the full 3D model. In particular, the 2D model is able to capture how the frequency splitting between the bonding and antibonding bands is reduced as $s$ increases, until reaching full degeneration of the bands for $s = d/2$.

Thus, to gain further insight into the physical origin of the observed geometrically induced degeneration, we have studied the evolution of the field profiles as a function of $s$. Figures 3(a) and 3(b) display the $H$-polarized magnetic field profiles (with **H** pointing along the $y$ direction), as computed at $k = \pi/d$ for the bonding and antibonding bands, respectively. The results for different values of $s$, going from $s = 0$ (leftmost panel) to $s = d/2$ (rightmost panel), are rendered in both panels of the figure.

As seen in the leftmost panels of Figs. 3(a) and 3(b), for $s = 0$ we obtain the canonical symmetric and asymmetric (with respect to the $z$ axis) field distributions associated with the bonding and antibonding band states, respectively. As expected, the presence of a nodal line along the $z$ axis causes the antibonding state to feature a significantly larger frequency than that corresponding to the bonding state. However, when we start shifting one of the CSP structures laterally with respect to the other, we significantly distort the field distribution of the corresponding bonding and antibonding states. Specifically, the significant perturbation of the fields observed at the center of the unit cell has two important effects. On one hand, it frustrates the formation of the horizontal nodal line of the antibonding state, lowering its frequency. On the other hand, by breaking the symmetry along the $x$ axis, it forces the bonding state to redistribute its field in a nonsymmetrical way around the grooves of the metallic combs. This in turn leads to an increase in the frequency of the corresponding mode. As shown in Figs. 3(a) and 3(b), the evolution of the field profiles and the corresponding frequencies follows this trend monotonically until the value of $s$ reaches $s = d/2$. At that value of the lateral shift, the symmetry of system forces the bonding and antibonding states to have exactly the same field distribution, and therefore the same frequency, as predicted by the symmetry arguments provided above. We note that although both states have the same field distribution, the corresponding Poynting vectors point in opposite directions [see the corresponding vectorial field distributions in the rightmost panels in Figs. 3(a) and 3(b)].

Finally, we have studied the modal field profiles of the full 3D version of the waveguiding structure shown in Fig. 1(a). In order to do that, we have carried out 3D simulations of an 80-period coupled CSP waveguide system. Perfectly matched absorbing boundary conditions have been employed at one of the waveguide ends to mimic an infinitely large waveguide. In addition, to ensure that a proper mode excitation is achieved in the waveguide, we launch through its input end a propagating mode featuring the modal profile and the $k$ value of the

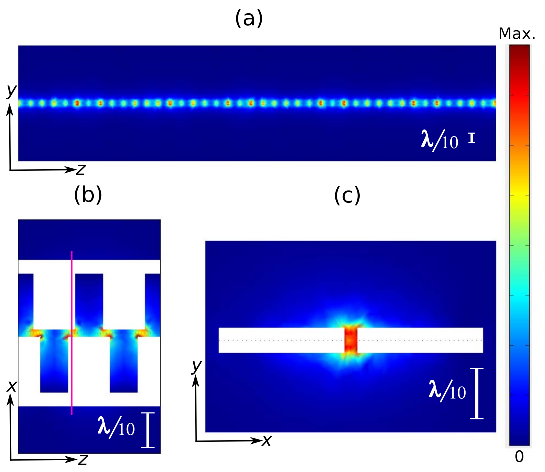


Fig. 4. Transversal cuts of the electric field norm computed for an 80-period-long waveguide based on the structure sketched in Fig. 1(a). The results along the (a) $z$–$y$, (b) $z$–$x$, and (c) $x$–$y$ planes are displayed. $s = d/2$ and $t = 0.2d$ are assumed in the calculations. The rest of geometrical parameters are the same as in Fig. 1(c). For clarity, (a) and (b) only render, respectively, 20-period and 2-periods sections of the whole waveguide. Part (c) shows the transversal cut along the pink line included in (b). All the displayed results were computed at a normalized carrier frequency $d/\lambda = 0.218$ (corresponding to the $k = \pi/d$ eigenmode of an infinitely periodic structure). The white areas in the plots represent PEC regions.

corresponding eigenmode computed for $k = \pi/d$ (the corresponding carrier frequency being $d/\lambda = 0.218$). The obtained results are summarized in Fig. 4. Figures 4(a)–4(c) display cross sections of the electric field norm $|\mathbf{E}|$ along the $z$–$y$, $z$–$x$, and $x$–$y$ planes, respectively. The deep-subwavelength $E$-field confinement featured by the guided mode is apparent from these results. To quantitatively characterize this confinement, we have computed the modal size $\delta$ of the waveguide mode. The parameter $\delta$ is defined as the transversal size of the circular area centered in the structure that concentrates 70% of total power carried by the system. A value of $\delta \approx \lambda/10$ is obtained in the transverse $x$–$y$ plane displayed in Fig. 4(c). This result corroborates the ability of the presented waveguides to simultaneously feature negative-index behavior and deep-subwavelength lateral confinement.

In summary, we have presented a novel route to achieve negative-index waveguiding at deep-subwavelength scales that exploits the symmetry properties that characterize the considered class of structures. These results could contribute to the development of surface circuitry for microwave and terahertz radiation.

We acknowledge financial support by the ERC Grant No. 290981 (PLASMONANOQUANTA) and the Spanish government (Grants CSD2007-046-Nanolight.es and MAT2011-28581-C02-01).

**References and Notes**

1. J. B. Pendry, L. Martín-Moreno, and F. J. García-Vidal, Science **305**, 847 (2004).
2. F. J. García-Vidal, L. Martín-Moreno, and J. B. Pendry, J. Opt. A **7**, S97 (2005).
3. A. P. Hibbins, B. R. Evans, and J. R. Sambles, Science **308**, 670 (2005).
4. F. J. García de Abajo and J. J. Sáenz, Phys. Rev. Lett. **95**, 233901 (2005).
5. C. R. Williams, S. R. Andrews, S. A. Maier, A. I. Fernández-Domínguez, L. Martín-Moreno, and F. J. García-Vidal, Nat. Photonics **2**, 175 (2008).
6. N. Yu, Q. J. Wang, M. A. Kats, J. A. Fan, S. P. Khanna, L. Li, A. G. Davies, E. H. Linfield, and F. Capasso, Nat. Mater. **9**, 730 (2010).
7. D. Martin-Cano, M. L. Nesterov, A. I. Fernandez-Domínguez, F. J. García-Vidal, L. Martín-Moreno, and E. Moreno, Opt. Express **18**, 754 (2010).
8. Y. J. Zhou, Q. Jiang, and T. J. Cui, Appl. Phys. Lett. **99**, 111904 (2011).
9. A. Pors, E. Moreno, L. Martín-Moreno, J. B. Pendry, and F. J. García-Vidal, Phys. Rev. Lett. **108**, 223905 (2012).
10. E. M. G. Brock and A. P. Hibbins, Appl. Phys. Lett. **103**, 111904 (2013).
11. X. Gao, J. H. Shi, X. Shen, H. F. Ma, W. X. Jiang, L. Li, and T. J. Cui, Appl. Phys. Lett. **102**, 151912 (2013).
12. D. Woolf, M. A. Kats, and F. Capasso, Opt. Lett. **39**, 517 (2014).
13. N. Yu and F. Capasso, Nat. Mater. **13**, 139 (2014).
14. X. Shen, T. J. Cui, D. Martin-Cano, and F. J. Garcia-Vidal, Proc. Natl. Acad. Sci. USA **110**, 40 (2013).
15. H. F. Ma, X. Shen, Q. Cheng, W. X. Jiang, and T. J. Cui, Laser Photon. Rev. **8**, 146 (2014).
16. J. B. Pendry, Phys. Rev. Lett. **85**, 3966 (2000).
17. R. A. Shelby, D. R. Smith, and S. Schultz, Science **292**, 77 (2001).
18. J. Valentine, S. Zhang, T. Zentgraf, E. Ulin-Avila, D. A. Genov, G. Bartal, and X. Zhang, Nature **455**, 376 (2008).
19. V. M. Shalaev, Nat. Photonics **1**, 41 (2007).
20. C. M. Soukoulis and M. Wegener, Nat. Photonics **5**, 523 (2011).
21. H. Shin and S. Fan, Phys. Rev. Lett. **96**, 073907 (2006).
22. H. J. Lezec, J. A. Dionne, and H. A. Atwater, Science **316**, 430 (2007).
23. E. Verhagen, R. de Waele, L. Kuipers, and A. Polman, Phys. Rev. Lett. **105**, 223901 (2010).
24. A. Hessel, N. Y. Farmingdale, M. H. Chen, R. C. M. Li, and A. A. Oliner, Proc. IEEE **61**, 183 (1973).
25. A. Hessel and A. A. Oliner, in *Electromagnetic Wave Theory*, J. Brown, ed. (Pergamon, 1965), pp. 251–260.
26. We have used the commercial software COMSOL Multiphysics.